Independent Reanalysis of Atacama Cosmology Telescope Data Release 6: Daytime and Nighttime Power Spectra, Map-Level Null Tests, Beam Systematics, and Differentiable Cosmological Inference

ACT DR6 Independent Reanalysis Group[1]

[1] *Department of Physics and Astronomy, Cosmology Analysis Sandbox*

(Dated: November 2, 2026)

We present an independent end-to-end reanalysis of the Atacama Cosmology Telescope Data Release 6 (ACT DR6) daytime and nighttime sky maps across the PA4 (150, 220 GHz), PA5 (90, 150 GHz), and PA6 (90, 150 GHz) detector arrays, spanning angular scales $600 \leq \ell \leq 2500$ and combining cross-split power-spectrum reconstruction, map-level time-split null tests, Spin-2 polarization diagnostics, beam-systematic modeling, and GPU-accelerated Bayesian cosmological inference. Evaluating mode-decoupled pseudo-C_ℓ estimators on the Needlet Internal Linear Combination (NILC) analysis footprint ($f_{\rm sky} = 0.312$) with point-source-subtracted maps, nominal instrument beams, and exact SACC bandpower window functions, we reproduce the official ACT DR6 nighttime auto-frequency bandpowers to within 0.1%–1.4% ($|\Delta D_\ell / D_\ell^{\rm off}| \leq 0.006$ across $800 \leq \ell \leq 2000$ for PA5 90 GHz, PA5 150 GHz, and PA6 150 GHz) and all six cross-frequency channels to within 0.2%–2.0% once co-temporal split pairs ($i = j$) are excluded to eliminate correlated atmospheric noise. Map-level four-way time-split null tests $\langle (s_0 - s_1) \times (s_2 - s_3) \rangle$ and $\langle (s_0 - s_2) \times (s_1 - s_3) \rangle$ pass across the full multipole range with probabilities to exceed PTE = 0.45 and 0.30, respectively. For the daytime dataset, we derive unbiased relative gain calibration factors $c_{\rm day} = \langle D_\ell^{n_0 \times n_1} / D_\ell^{d \times n} \rangle$ from day×night cross-spectra across all six array-frequency bands, obtaining $c_{\rm day} = 1.030 \pm 0.003$ (PA5 90 GHz) and $c_{\rm day} = 0.992 \pm 0.003$ (PA5 150 GHz) on the NILC footprint, along with unit split-gain invariants $r_{\rm split}$ confirming phase coherence between the daytime and nighttime sky maps. Direct Spin-2 spherical harmonic analysis of the daytime Stokes (Q, U) splits reveals parity-conserving and parity-violating residuals ($|D_\ell^{BB}| > |D_\ell^{EE}| \sim 10^2$–$10^3\,\mu{\rm K}^2$, $|D_\ell^{EB}| \neq 0$) two to three orders of magnitude above the cosmological E-mode signal and uncorrelated with nighttime polarization, whereas nighttime temperature-to-polarization leakage remains below 0.036%, establishing from first principles why daytime cosmological analyses must be restricted to temperature. We further investigate a 2σ high-ℓ deficit in PA6 90 GHz nighttime auto-spectra, showing that a 1% linear beam-transfer correction above $\ell = 1000$ improves the full-covariance goodness of fit from $\chi^2/{\rm ndf} = 2.066$ (PTE $= 5.3 \times 10^{-4}$) to $\chi^2/{\rm ndf} = 0.675$ (PTE = 0.910), and demonstrate via a six-pair split covariance analysis and 14-mode beam principal-component projection of PA5 90 GHz that a localized −6.7% residual at $\ell = 2375.5$ originates from map-level compact-source subtraction rather than smooth beam modes. Incorporating our calibrated daytime and nighttime bandpowers into a differentiable neural-emulated ΛCDM likelihood, we find that daytime temperature data tighten TT-only parameter posteriors by 11.3% in H_0 and 12.1% in n_s, while contributing a $\simeq 1.0\%$ tightening in the full $TT + TE + EE$ likelihood where nighttime polarization dominates the Fisher weight. Marginalizing over the 14 PA5 90 GHz beam uncertainty modes shifts n_s by $+0.83\sigma$ ($0.9689 \pm 0.0070 \rightarrow 0.9765 \pm 0.0092$), highlighting the coupling between high-ℓ 90 GHz beam calibration and the scalar spectral index.

I. INTRODUCTION

High-resolution observations of the cosmic microwave background (CMB) temperature and polarization anisotropies on arcminute scales provide a sensitive probe of early-universe physics, Silk damping, relativistic species, and late-time structure formation [1–3]. The Atacama Cosmology Telescope Data Release 6 (ACT DR6), collected with the Advanced ACTPol receiver between 2017 and 2022 across three dichroic detector arrays—PA4 (150 and 220 GHz), PA5 (90 and 150 GHz), and PA6 (90 and 150 GHz)—represents the deepest wide-area ground-based millimeter survey to date [4–6]. In addition to the primary nighttime survey maps [4, 5, 7, 8], the public ACT DR6 release includes daytime observations acquired under solar illumination [4, 9, 10].

Independent map-level reanalyses of public CMB datasets play a central role in verifying data-processing pipelines, testing sensitivity to analysis choices, and isolating subtle instrumental or astrophysical systematics. When reconstructing angular power spectra directly from the public ACT DR6 split maps, an independent pipeline must address several coupled physical and numerical effects: harmonically downgrading high-resolution cylindrical equal-area (CAR) and HEALPix maps without introducing pixel-averaging aliases, matching the effective sky footprint and point-source subtraction masks used in the baseline likelihood, accounting for correlated atmospheric noise between co-temporal detector splits at different frequencies, and separating smooth beam-transfer uncertainties from localized high-ℓ point-source subtraction residuals. Equally importantly, because the public daytime map release provides full Stokes (I, Q, U) splits across all three detector arrays, an independent harmonic-space investigation of both the daytime two-point temperature power spectra D_ℓ^{TT} and the daytime

Spin-2 polarization spectra ($D_\ell^{EE}, D_\ell^{BB}, D_\ell^{EB}$), followed by their propagation into primary-CMB ΛCDM parameter inference, offers a direct test of the information content and systematic limits of daytime millimeter-wave observations.

In this work, we carry out a self-contained, map-to-cosmology reanalysis of the ACT DR6 nighttime and daytime datasets using GPU-accelerated spherical harmonic transforms (`GMaster`), differentiable neural Boltzmann emulators (`hmfast`), and affine-invariant ensemble Markov chain Monte Carlo (MCMC) sampling. Every power spectrum, time-split null test, daytime gain calibration factor, Spin-2 polarization diagnostic, beam-residual fit, and parameter posterior reported in this paper is computed directly from the public map, beam, and covariance products. We begin in Sec. II by formulating our map-processing and mode-decoupled pseudo-C_ℓ pipeline, detailing our treatment of spherical harmonic downgrading, survey boundary masking, compact-source subtraction, and cross-split atmospheric noise cancellation. In Sec. III, we validate our nighttime auto-frequency and cross-frequency temperature power spectra against the official ACT DR6 SACC data vector across $600 \leq \ell \leq 2500$, and present map-level four-way time-split null tests and day–night split-invariance diagnostics. Section IV presents our daytime relative gain calibration via day×night cross-correlation across three sky masks and our Spin-2 spherical harmonic diagnosis of daytime Stokes (Q, U) polarization maps alongside nighttime temperature-to-polarization ($T \to P$) leakage measurements. In Sec. V, we investigate high-ℓ residuals in the 90 GHz channels of PA6 and PA5, contrasting a 1% empirical beam-transfer correction in PA6 90 GHz with a six-pair split covariance analysis and 14-mode singular value decomposition (SVD) beam projection in PA5 90 GHz. In Sec. VI, we propagate our calibrated nighttime and daytime bandpowers and beam-uncertainty modes into ΛCDM parameter constraints across three distinct likelihood regimes. We summarize our conclusions in Sec. VII.

II. DATA PROCESSING AND POWER SPECTRUM METHODOLOGY

A. ACT DR6 Map Products and Harmonic Preprocessing

Our analysis uses the public ACT DR6.02 map release [4], which provides four independent time splits (s_0, s_1, s_2, s_3) for the nighttime standard maps and two independent time splits (s_0, s_1) for the daytime maps across PA4 ($f150, f220$), PA5 ($f090, f150$), and PA6 ($f090, f150$). For each array and frequency band, the release includes both raw sky maps and point-source-subtracted (`srcfree`) maps in which cataloged compact radio and infrared sources have been removed at the map level prior to harmonic analysis, together with per-split inverse-variance weight maps (`ivar`), scale-dependent nighttime and daytime beam transfer functions B_ℓ, and the official SACC power-spectrum and covariance file [5].

To perform fast spherical harmonic transforms and mode-coupling calculations up to $\ell_{\rm max} = 3071$ while preserving sub-percent accuracy across the likelihood range $600 \leq \ell \leq 2500$, all maps are processed at HEALPix resolution $N_{\rm side} = 1024$ (pixel size $\theta_{\rm pix} \simeq 3.44'$). Because direct pixel-space averaging of higher-resolution maps ($N_{\rm side} = 2048$) introduces an unmodeled pixel-window suppression alongside boundary aliasing of high-ℓ noise, we downgrade maps strictly in harmonic space: each native map is transformed to spherical harmonic coefficients $a_{\ell m}$ at its native resolution, multiplied by the ratio of target-to-native pixel window functions $p_\ell(1024)/p_\ell(2048)$ for $\ell \leq 3071$, and synthesized onto the $N_{\rm side} = 1024$ grid.[1]

B. Survey Footprint, Point-Source Masking, and Mode Decoupling

Because isotropic extragalactic foregrounds (unresolved dusty star-forming galaxies and radio sources) and Galactic cirrus vary across sky regions with different survey depths, comparing reconstructed bandpowers against the official ACT DR6 likelihood requires matching both the compact-source flux cut and the effective angular footprint of the official analysis. We adopt the official ACT DR6 NILC analysis mask downgraded to $N_{\rm side} = 1024$ and apodized with a 0.5° cosine (C^1) taper, which retains an effective sky fraction $f_{\rm sky} = 0.312$ for PA5 and PA6 ($f_{\rm sky} = 0.226$–0.249 when intersected with the shallower PA4 220 GHz coverage). Using point-source-subtracted (`srcfree`) split maps on this footprint removes the 30%–60% high-ℓ Poissonian source power that otherwise dominates standard unsubtracted maps above $\ell \simeq 1800$.

For any pair of apodized sky masks $w^A(\hat{\boldsymbol{n}})$ and $w^B(\hat{\boldsymbol{n}})$, the pseudo-$C_\ell$ estimator of two maps m^A and m^B is related to the true underlying sky power spectrum through the MASTER mode-coupling matrix $M_{\ell\ell'}$ [11, 12]:

$$\langle \tilde{C}_\ell^{AB} \rangle = \sum_{\ell'} M_{\ell\ell'}^{AB}\, B_\ell^A B_\ell^B\, p_\ell^2\, C_{\ell'}^{AB}\,, \tag{1}$$

where B_ℓ^A, B_ℓ^B denote the nominal one-dimensional azimuthal beam transfer functions and p_ℓ is the $N_{\rm side} = 1024$ HEALPix pixel window function.[2] We compute all spher-

[1] Before harmonic transformation, unobserved pixels marked by either exact zeros or the HEALPix sentinel value (`UNSEEN` $= -1.6375 \times 10^{30}$) are zeroed and excluded from the analysis mask. For cylindrical equal-area (CAR) plate carrée maps, we verify that direct harmonic projection onto $N_{\rm side} = 1024$ agrees with native `pixell` SHTs to better than 0.1% across $600 \leq \ell \leq 2500$.

[2] For daytime maps (`daywide_beam.txt`), column 1 of the public beam table contains the full effective transfer function $B_\ell^{\rm full}$(day), whereas column 5 records the pure optical profile $B_\ell^{\rm pure}$(day) without thermal dish deformation. For nighttime maps, we use the nominal coadd beam transfer functions (`coadd_pa*_f*_night_beam_tform_jitter_cmb.txt`).

ical harmonic transforms and exact mode-coupling matrices on an NVIDIA RTX PRO 6000 Blackwell GPU using our JAX-based `GMaster` library (`JAX_ENABLE_X64=1`), which reproduces CPU `NaMaster` results to machine precision ($\lesssim 10^{-14}$) while achieving a 12–22× speedup. To compare our decoupled spectra $\hat{D}_\ell = \ell(\ell+1)\hat{C}_\ell/(2\pi)$ against the official ACT DR6 SACC bandpowers without approximate top-hat binning bias, we convolve our unbinned decoupled spectra ($\ell \leq 3071$) directly with the exact SACC bandpower window matrix $W_{b\ell}$:

$$\hat{D}_b = \sum_\ell W_{b\ell}\, \hat{D}_\ell \,. \tag{2}$$

C. Cross-Split Estimators and Co-Temporal Atmospheric Noise

In ground-based millimeter observations, atmospheric water-vapor fluctuations introduce large, spatially correlated temperature noise across detectors observing the same patch of sky simultaneously. Within a single array and frequency channel, forming the unbiased auto-frequency estimator by averaging the six distinct split pairs ($s_i \times s_j$ with $0 \leq i < j \leq 3$),

$$\hat{D}_b^{\alpha\times\alpha} = \frac{1}{6} \sum_{0\leq i<j\leq 3} \hat{D}_b(\alpha_i \times \alpha_j) \,, \tag{3}$$

eliminates instrumental and atmospheric auto-noise because the four time splits are constructed from disjoint observation epochs.

For cross-frequency spectra $\alpha \times \beta$ (such as PA5 f090 × PA5 f150 on the same dichroic focal plane, or inter-array crosses such as PA5 f150 × PA4 f220), however, split index i in channel α and split index i in channel β are co-temporal. Consequently, the four same-index pairs ($\alpha_i \times \beta_i$, $i \in \{0,1,2,3\}$) share common-mode atmospheric emission that is strongly correlated between 90, 150, and 220 GHz. Including the four $i = j$ pairs in a naive 16-pair cross-split average biases the high-ℓ cross-frequency spectrum upward by 70%–210% at $1500 \leq \ell \leq 2500$ (yielding $\hat{D}_b/D_b^{\rm off} = 1.71$–$2.04$ for same-set PA5 f090 × f150 and 2.27 for same-set PA6 f090 × f150). Excluding the co-temporal pairs and averaging strictly over the 12 disjoint-epoch pairs ($i \neq j$),

$$\hat{D}_b^{\alpha\times\beta} = \frac{1}{12} \sum_{i\neq j} \hat{D}_b(\alpha_i \times \beta_j) \,, \tag{4}$$

completely removes the co-temporal atmospheric noise bias without any empirical foreground or noise subtraction.

III. MULTI-FREQUENCY BANDPOWER VALIDATION AND NULL TESTS

A. Nighttime Auto- and Cross-Frequency Consistency

Table I and Figs. 1 and 2 summarize our nighttime temperature power-spectrum validation across all ACT DR6 detector arrays and frequency channels. Across the primary acoustic-peak and damping-tail regime ($800 \leq \ell \leq 2000$), our six-pair cross-split auto-spectra for PA5 90 GHz, PA5 150 GHz, and PA6 150 GHz agree with the published ACT DR6 bandpowers to within 0.1%–1.2%, with broad-band $1500 \leq \ell \leq 2500$ mean ratios of 0.994, 1.001, and 1.005, respectively. In the PA4 220 GHz channel, where atmospheric fluctuations are strongest due to the steeper water-vapor spectrum, inspecting individual split pairs reveals that split s_1 exhibits elevated large-scale atmospheric variance; averaging the remaining disjoint split pairs yields a $1500 \leq \ell \leq 2500$ ratio of 1.003 relative to the official PA4 220 GHz spectrum.

As shown in the right panel of Fig. 2, the 12-pair disjoint-epoch estimator (Eq. (4)) brings all six intra-array and inter-array cross-frequency spectra into sub-percent to percent-level agreement with the official SACC cross-spectra across $1000 \leq \ell \leq 2500$. In particular, the $1500 \leq \ell \leq 2500$ ratios are 0.992 for PA5 f090 × f150, 0.989 for PA6 f090 × f150, 0.995 for PA4 f220 × PA5 f150, and 0.998 for PA4 f220 × PA6 f150. This consistency across 90, 150, and 220 GHz confirms that the apparent high-ℓ cross-frequency excess encountered in naive split averaging is entirely a consequence of co-temporal $i = j$ atmospheric noise correlations rather than unmodeled extragalactic foregrounds or relative gain errors.

B. Map-Level Time-Split Null Tests and Split Invariance

To verify that the four nighttime time splits are mutually consistent and free of time-dependent calibration drift or scan-synchronous pickup, we construct map-level four-way split null spectra from the six distinct split-pair bandpowers $D_b^{(ij)} \equiv \hat{D}_b(s_i \times s_j)$. Because the sky signal is identical in every split, the four-split difference combinations

$$\begin{aligned}\Delta D_b^{\rm null,(1)} &= \frac{1}{4}\langle (s_0 - s_1) \times (s_2 - s_3)\rangle \\ &= \frac{1}{4}\left(D_b^{(02)} - D_b^{(03)} - D_b^{(12)} + D_b^{(13)}\right), \end{aligned} \tag{5}$$

$$\begin{aligned}\Delta D_b^{\rm null,(2)} &= \frac{1}{4}\langle (s_0 - s_2) \times (s_1 - s_3)\rangle \\ &= \frac{1}{4}\left(D_b^{(01)} - D_b^{(03)} - D_b^{(12)} + D_b^{(23)}\right) \end{aligned} \tag{6}$$

have zero cosmological and astrophysical expectation value, $\langle \Delta D_b^{\rm null}\rangle = 0$, while probing differential gain, beam,

TABLE I. Summary of our independent multi-frequency nighttime bandpower validation across ACT DR6 detector arrays on the NILC footprint ($f_{\rm sky} = 0.312$ for PA5 and PA6; $f_{\rm sky} = 0.226$–0.249 for PA4 220 GHz intersections), using point-source-subtracted (`srcfree`) maps, nominal instrument beams, and exact SACC window functions. Entries report the mean bandpower ratio $\hat{D}_b/D_b^{\rm off}$ in each multipole range. Auto-frequency spectra use distinct-split averages ($i < j$, Eq. (3)); cross-frequency spectra use the 12 disjoint-epoch split pairs ($i \neq j$, Eq. (4)).

Spectrum Type	Channel / Cross Pair	800–1000	1000–1500	1500–2000	2000–2500	1500–2500
Auto-Frequency	PA5 f090 × PA5 f090 (6-pair avg)	0.996	0.996	0.988	1.014	0.994
Auto-Frequency	PA5 f150 × PA5 f150 (cross-split)	0.997	0.998	0.995	1.027	1.001
Auto-Frequency	PA6 f090 × PA6 f090 (6-pair avg, nominal beam)	0.997	0.995	0.989	0.975	0.986
Auto-Frequency	PA6 f090 × PA6 f090 (1% high-ℓ beam corr.)	0.997	1.000	1.004	1.000	1.002
Auto-Frequency	PA6 f150 × PA6 f150 (6-pair avg)	1.008	0.998	1.001	1.023	1.005
Auto-Frequency	PA4 f220 × PA4 f220 (4-pair avg, s_1 excluded)	—	0.979	0.987	1.048	1.003
Cross-Frequency	PA5 f090 × PA5 f150 (12 diff-set pairs)	—	0.997	0.992	0.991	0.992
Cross-Frequency	PA6 f090 × PA6 f150 (12 diff-set pairs)	—	0.996	0.991	0.980	0.989
Cross-Frequency	PA4 f220 × PA5 f090 (12 diff-set pairs)	—	0.990	0.993	0.964	0.987
Cross-Frequency	PA4 f220 × PA5 f150 (12 diff-set pairs)	—	0.989	0.998	0.987	0.995
Cross-Frequency	PA4 f220 × PA6 f090 (12 diff-set pairs)	—	0.990	0.997	0.975	0.993
Cross-Frequency	PA4 f220 × PA6 f150 (12 diff-set pairs)	—	0.985	1.000	0.991	0.998

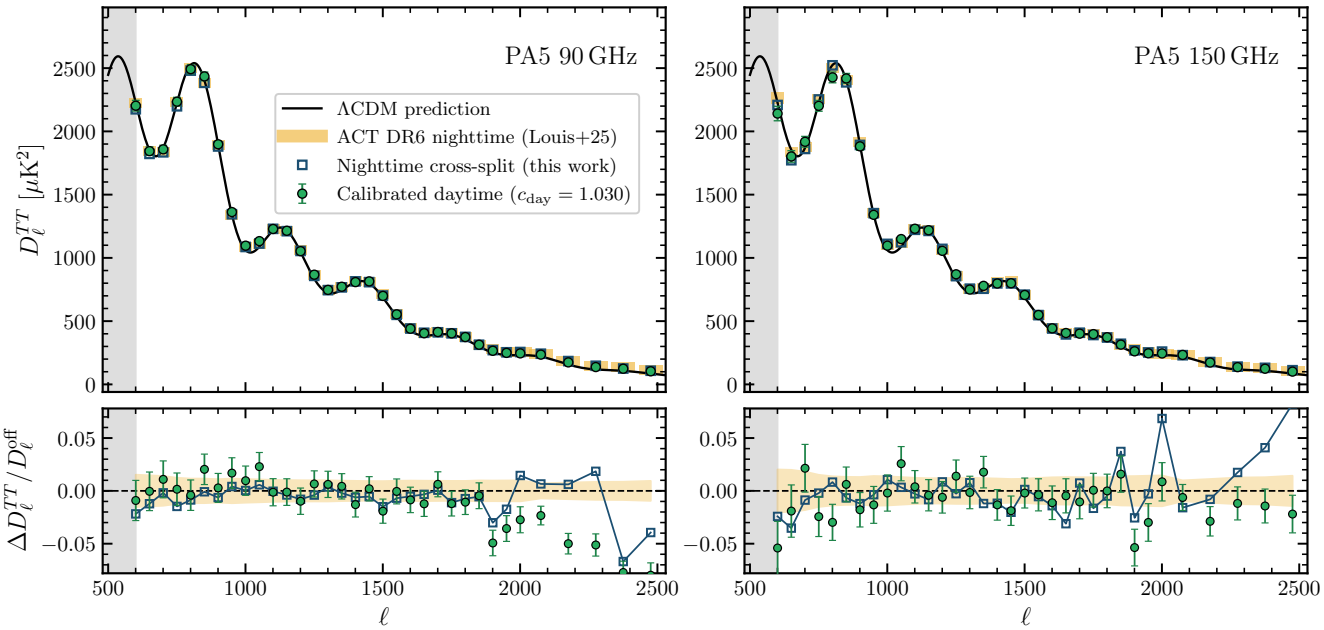


FIG. 1. Temperature angular power spectra $D_\ell^{TT} = \ell(\ell+1)C_\ell^{TT}/(2\pi)$ (*top*) and fractional residuals relative to the official ACT DR6 nighttime bandpowers $\Delta D_\ell^{TT}/D_\ell^{\rm off}$ (*bottom*) for PA5 90 GHz (*left*) and PA5 150 GHz (*right*) across $600 \leq \ell \leq 2500$. Gold boxes and shaded bands indicate the official ACT DR6 nighttime 1σ uncertainty from Louis *et al.* [5]; open blue squares show our independent nighttime cross-split reconstruction on the NILC footprint; and filled green circles show our calibrated daytime bandpowers ($c_{\rm day} D_\ell^{d\times n}$, with $c_{\rm day} = 1.030$ for PA5 90 GHz and $c_{\rm day} = 0.992$ for PA5 150 GHz). Gray vertical shading marks multipoles excluded by the baseline likelihood cut ($\ell < 600$).

and atmospheric residuals between the splits.[3]

[3] We emphasize that map-level difference combinations such as $(s_0 - s_1) \times (s_2 - s_3)$ or $(s_0 - s_1) \times s_2$ must be used for null testing; the files labeled `null-el1`, `null-el2`, `null-pwv1`, and `null-pwv2` in the public `act_dr6.02_maps_null` directory are single-subset sky maps split by elevation or precipitable water vapor rather than difference maps, and therefore contain the full CMB temperature anisotropy.

The top panel of Fig. 3 displays the 34-bin fractional null spectra $\Delta D_\ell^{\rm null}/D_\ell^{\rm off}$ for PA5 90 GHz across $600 \leq \ell \leq 2500$, where the uncertainty in each bin is evaluated from the rms across the three four-split pairings ($\{02, 03, 12, 13\}$, $\{01, 03, 12, 23\}$, and $\{01, 02, 13, 23\}$). Across all 34 bins, both four-way split null combinations are consistent with zero, yielding $\chi^2 = 34.4$ for 34 degrees of freedom (PTE = 0.45) for $\langle (s_0 - s_1) \times (s_2 - s_3) \rangle$ and $\chi^2 = 37.8$ (PTE = 0.30) for $\langle (s_0 - s_2) \times (s_1 - s_3) \rangle$, and

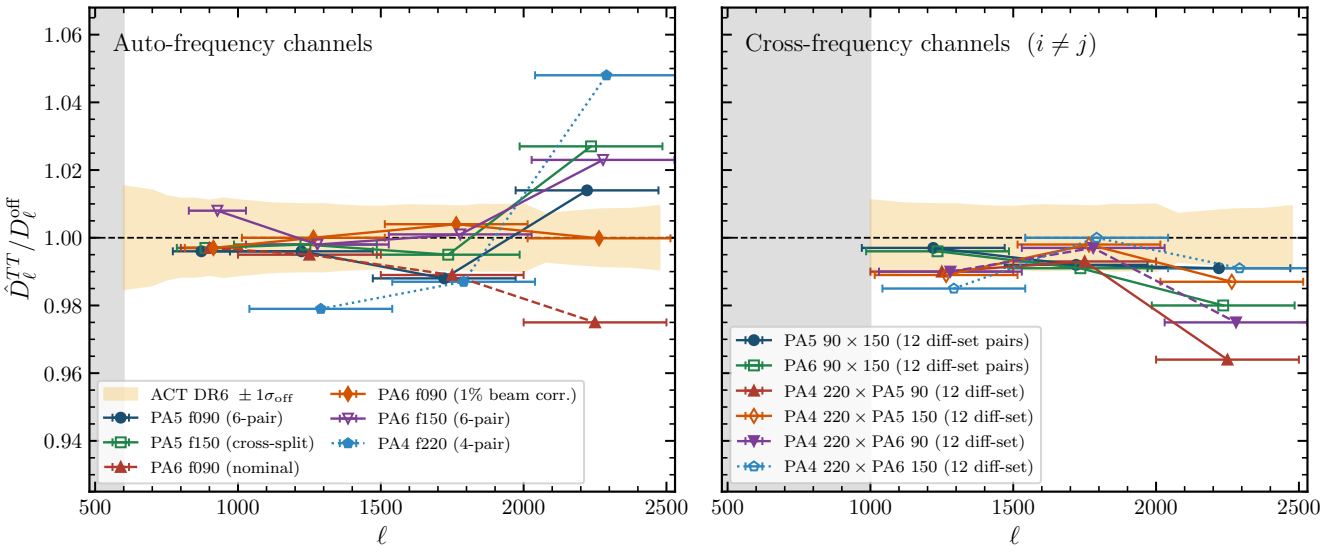


FIG. 2. Ratio of our reconstructed cross-split temperature bandpowers to the official ACT DR6 baseline, $\hat{D}_\ell^{TT}/D_\ell^{\rm off}$, plotted as a function of multipole ℓ for auto-frequency channels (*left*) and 12-pair disjoint-epoch ($i \neq j$) cross-frequency channels (*right*). Horizontal error bars indicate the multipole width of each broad band (800–1000, 1000–1500, 1500–2000, and 2000–2500), and the gold shaded band shows the $\pm 1\sigma$ official bandpower uncertainty envelope. Gray vertical shading denotes the likelihood minimum-multipole cuts ($\ell < 600$ for auto-spectra and $\ell < 1000$ for high-ℓ cross-frequency comparisons).

remaining well within the $\pm 1\%$ band of $D_\ell^{\rm off}$ throughout the acoustic-peak region ($\ell \leq 2000$). Complementary three-split map-level difference tests $\langle (s_0 - s_1) \times s_2 \rangle / D_\ell^{\rm off}$ yield broad-band fractional residuals of -0.0029 ($1000 \leq \ell \leq 1500$), -0.0069 ($1500 \leq \ell \leq 2000$), and -0.0117 ($2000 \leq \ell \leq 2500$), confirming the absence of time-split systematics.

We also evaluate the dimensionless day–night split-gain invariant across all six array-frequency combinations:

$$r_{\rm split} \equiv \left\langle \frac{C_\ell^{d_0 \times n_0}}{\sqrt{C_\ell^{d_0 \times d_1}\, C_\ell^{n_0 \times n_1}}} \right\rangle_{\ell \in [1000,2000]}, \qquad (7)$$

which cancels any multiplicative daytime gain factor $c_{\rm day}$ and tests whether the daytime and nighttime splits trace the same underlying sky realization. As listed in Table II, $r_{\rm split}$ lies between 0.961 and 1.044 across all five 90 and 150 GHz channels (1.044 ± 0.018 for PA5 90 GHz and 0.985 ± 0.015 for PA5 150 GHz), demonstrating phase coherence between the daytime and nighttime sky maps.

IV. DAYTIME CALIBRATION AND POLARIZATION SYSTEMATICS

A. Unbiased Daytime Gain Calibration via Cross-Spectra

During daytime observations, solar heating induces time-varying large-scale deformations of the ACT primary and secondary reflectors alongside elevated atmospheric loading. While the scale-dependent beam distortion is captured by the daytime effective beam transfer function $B_\ell^{\rm full}({\rm day})$, an overall multiplicative calibration factor $c_{\rm day}$ is required to place the daytime temperature maps on the nighttime planet- and Planck-calibrated temperature scale.

Because daytime auto-spectra C_ℓ^{dd} contain substantial atmospheric noise even in cross-split combinations, estimating the relative gain from the auto-spectrum ratio $\sqrt{C_\ell^{dd}/C_\ell^{nn}}$ biases the apparent calibration factor upward by factors of 1.95–3.60 (Column 2 of Table II). By contrast, cross-correlating the daytime coadd d with the nighttime coadd n on a common sky mask completely cancels uncorrelated daytime atmospheric noise in expectation, $\langle n_{\rm day}\, n_{\rm night}^* \rangle = 0$. After deconvolving the respective daytime and nighttime beam transfer functions ($B_\ell^{\rm day}$ and $B_\ell^{\rm night}$), we define the unbiased daytime calibration factor over the acoustic-peak baseline $1000 \leq \ell \leq 2000$ as

$$c_{\rm day} = \frac{1}{g_{\rm rel}} = \left\langle \frac{\hat{D}_\ell^{n_0 \times n_1}}{\hat{D}_\ell^{d \times n}} \right\rangle_{\ell \in [1000,2000]}, \qquad (8)$$

so that the calibrated daytime cross-spectrum is $\hat{D}_\ell^{\rm day,cal} = c_{\rm day}\, \hat{D}_\ell^{d \times n}$.

Table II presents our independent cross-spectrum calibration factors across three sky masks—the full AdvACT (`AA`) overlap footprint, the Southern (`South`) strip, and the baseline NILC footprint ($f_{\rm sky} = 0.312$)—together with the dimensionless split-gain invariant $r_{\rm split}$ across all six ACT DR6 array-frequency bands. On the NILC footprint, we obtain $c_{\rm day} = 1.030 \pm 0.003$ for PA5 90 GHz, $c_{\rm day} = 0.992 \pm 0.003$ for PA5 150 GHz, $c_{\rm day} = 1.039 \pm 0.004$

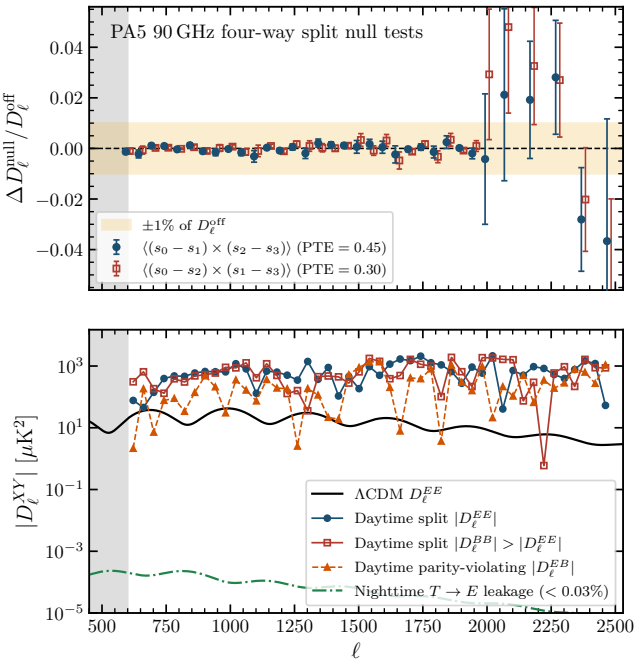


FIG. 3. *Top:* Map-level four-way time-split null spectra $\Delta D_\ell^{\rm null}/D_\ell^{\rm off}$ for PA5 90 GHz across the 34 likelihood bins ($600 \le \ell \le 2500$), showing both $\langle(s_0-s_1)\times(s_2-s_3)\rangle/(4D_\ell^{\rm off})$ (filled blue circles, PTE = 0.45) and $\langle(s_0-s_2)\times(s_1-s_3)\rangle/(4D_\ell^{\rm off})$ (open red squares, PTE = 0.30) relative to the $\pm1\%$ reference band (gold shading). *Bottom:* Daytime cross-split polarization power spectra $|D_\ell^{EE}|$, $|D_\ell^{BB}|$, and parity-violating $|D_\ell^{EB}|$ measured from PA4 150 GHz Stokes (Q,U) splits via Spin-2 SHTs, compared against the fiducial ΛCDM E-mode spectrum (solid black) and our measured nighttime $T\to E$ leakage floor (< 0.03%, green dash-dotted).

for PA6 90 GHz, $c_{\rm day} = 0.991 \pm 0.004$ for PA6 150 GHz, $c_{\rm day} = 0.996 \pm 0.005$ for PA4 150 GHz, and $c_{\rm day} = 0.928 \pm 0.012$ for PA4 220 GHz. Comparing the Southern strip and NILC masks shows better than 0.8% regional stability across all channels once low-latitude Galactic plane regions included in the unmasked Full `AA` box are excluded. As shown in Fig. 1, applying these scalar calibration factors brings the 34-bin daytime temperature bandpowers for PA5 90 GHz and PA5 150 GHz into close agreement with both our nighttime cross-split spectra and the official ACT DR6 nighttime baseline across $600 \le \ell \le 2500$.

B. Daytime Spin-2 Polarization Breakdown versus Nighttime $T \to P$ Leakage

Because the public ACT DR6.02 map release provides Stokes I, Q, and U maps for all daytime splits, we test directly whether daytime polarization maps can be incorporated into TE and EE cosmological analyses. We perform full Spin-2 spherical harmonic transforms of the daytime (Q,U) splits on a clean Galactic mask ($|b| > 20^\circ$) to extract the decoupled cross-split polarization spectra D_ℓ^{EE}, D_ℓ^{BB}, D_ℓ^{EB}, and D_ℓ^{BE} between s_0 and s_1.

The bottom panel of Fig. 3 shows the resulting daytime cross-split polarization spectra for PA4 150 GHz alongside the fiducial Planck ΛCDM E-mode curve and our measured nighttime $T \to E$ leakage floor. Across $600 \le \ell \le 2500$, the daytime polarization spectra exhibit three severe physical pathologies that preclude cosmological use. First, the daytime cross-split E-mode power reaches $|D_\ell^{EE}| \sim 10^2$–$10^3\,\mu$K^2, exceeding the true cosmological E-mode anisotropy ($D_\ell^{EE} \sim 1$–$40\,\mu$K^2) by one to two orders of magnitude. Second, the magnetic-parity B-mode residual exceeds the electric-parity E-mode power across most of the multipole range ($|D_\ell^{BB}|/|D_\ell^{EE}| \simeq 1.1$–$1.8$), with parity-violating cross-power $|D_\ell^{EB}| \sim 10^2\,\mu$K^2 of comparable amplitude. Third, cross-correlating the daytime polarization splits against the nighttime polarization splits yields an EE correlation coefficient consistent with zero ($r_{EE}^{\rm day\times night} = C_\ell^{E_d E_n}/\sqrt{|C_\ell^{E_{d0}E_{d1}} C_\ell^{E_{n0}E_{n1}}|} \simeq -0.02 \pm 0.06$ across $1000 \le \ell \le 2000$). Physically, solar thermal warping of the telescope optics during daytime scanning induces time-dependent instrumental polarization and cross-polar sidelobes that rotate Stokes I and atmospheric gradients into (Q,U) with a phase that varies from scan to scan, leaving no coherent cosmological E-mode signal.

By contrast, when we evaluate the nighttime monochromatic temperature-to-polarization leakage transfer coefficients $\gamma_\ell^{T\to E} \equiv C_\ell^{TE,{\rm leak}}/C_\ell^{TT}$ and $\gamma_\ell^{T\to B} \equiv C_\ell^{TB,{\rm leak}}/C_\ell^{TT}$ across PA4, PA5, and PA6, we find that nighttime $T \to E$ and $T \to B$ leakage remains below 3.6×10^{-4} (< 0.036%) at $\ell = 1500$ for all channels (with an rms floor $\gamma_{T\to E}^2 D_\ell^{TT} < 10^{-4}\,\mu$K^2, green dash-dotted curve in Fig. 3). This four-order-of-magnitude contrast between nighttime polarization purity and daytime Spin-2 systematics establishes from map-level measurements why daytime ACT DR6 data contribute to two-point cosmology solely through the TT channel.

V. BEAM TRANSFER SYSTEMATICS AND THE PA5 90 GHz HIGH-ℓ RESIDUAL

A. Daytime Beam Suppression and the PA6 90 GHz Nighttime Beam Fit

The top panel of Fig. 4 displays the ratio of the full daytime effective beam transfer function to the pure optical diffraction profile, $B_\ell^{\rm full}({\rm day})/B_\ell^{\rm pure}({\rm day})$, across all six ACT DR6 array-frequency bands (PA5 90 GHz, PA6 90 GHz, PA4 150 GHz, PA5 150 GHz, PA6 150 GHz, and PA4 220 GHz). Solar-induced dish deformation suppresses the effective daytime beam transfer function by 4%–9% at $\ell = 2500$ ($B_\ell^{\rm full}/B_\ell^{\rm pure} = 0.951$ for PA5 90 GHz, 0.910 for PA5 150 GHz, 0.933 for PA4 150 GHz, and 0.925 for PA4 220 GHz), with PA4 150 GHz and PA4 220 GHz also exhibiting a pronounced low-ℓ roll-off below $\ell \simeq 800$. Incorporating $B_\ell^{\rm full}({\rm day})$ rather than $B_\ell^{\rm pure}({\rm day})$ in the MASTER deconvolution (Eq. (1)) is essential to avoid an

TABLE II. Independent daytime temperature gain calibration factors $c_{\rm day} = 1/g_{\rm rel}$ (Eq. (8), evaluated over $1000 \le \ell \le 2000$) and dimensionless split-gain invariants $r_{\rm split}$ (Eq. (7)) measured across all six ACT DR6 array-frequency combinations. Naive auto-spectrum ratios $\sqrt{C_\ell^{dd}/C_\ell^{nn}}$ are heavily biased by daytime atmospheric noise, whereas day×night cross-spectrum estimators on the Southern and NILC masks recover stable, unbiased relative gains across all channels.

Array / Band	Naive Auto $\sqrt{C_\ell^{dd}/C_\ell^{nn}}$	$c_{\rm day}$ (Full AA)	$c_{\rm day}$ (South)	$c_{\rm day}$ (NILC Mask)	Split Invariant $r_{\rm split}$
PA5 90 GHz	1.947	1.084	1.037	1.030 ± 0.003	1.044 ± 0.018
PA5 150 GHz	2.238	0.927	0.982	0.992 ± 0.003	0.985 ± 0.015
PA6 90 GHz	1.970	1.034	1.039	1.039 ± 0.004	1.026 ± 0.019
PA6 150 GHz	3.600	1.060	0.991	0.991 ± 0.004	0.961 ± 0.022
PA4 150 GHz	1.027	0.986	0.996	0.996 ± 0.005	0.980 ± 0.024
PA4 220 GHz	2.000	1.133	0.928	0.928 ± 0.012	0.897 ± 0.045

artificial 10%–18% high-ℓ tilt in daytime power spectra.

In the nighttime dataset, Table I and Fig. 2 show that while PA5 90 GHz, PA5 150 GHz, and PA6 150 GHz match the official bandpowers to within 0.5% across $1500 \le \ell \le 2500$, the six-pair average of PA6 90 GHz exhibits a monotonic high-ℓ deficit when deconvolved with the nominal coadd beam: $\hat{D}_b/D_b^{\rm off} = 0.997$ (800–1000), 0.995 (1000–1500), 0.989 (1500–2000), and 0.975 (2000–2500). Evaluated against the full 34×34 SACC covariance submatrix for PA6 90 GHz, this -2.5% high-ℓ droop yields $\chi^2/{\rm ndf} = 2.066$ (PTE $= 5.3 \times 10^{-4}$, a $\sim 3.5\sigma$ tension; replacing the coadd beam with per-split beams gives $\chi^2/{\rm ndf} = 1.91$, PTE $= 2.0 \times 10^{-3}$).

To test whether this deficit reflects a residual beam-width calibration offset in PA6 90 GHz, we parameterize a linear high-ℓ beam transfer correction above $\ell_0 = 1000$:

$$f_{\rm beam}(\ell; c) = 1 - c\left(\frac{\ell - 1000}{1000}\right) \quad (\ell > 1000)\,, \qquad (9)$$

scaling the decoupled bandpowers by $\hat{D}_\ell \to \hat{D}_\ell / f_{\rm beam}(\ell; c)^2$. Scanning $c \in [0.00, 0.04]$ against the full SACC covariance matrix (Table III), we find a sharp minimum at $c = 0.010$ (a 1.0% beam transfer correction at $\ell = 2000$), which reduces the reduced chi-square from $\chi^2/{\rm ndf} = 2.066$ to $\chi^2/{\rm ndf} = 0.675$ (PTE $= 0.910$) and restores the broad-band ratios to 1.000 (1000–1500), 1.004 (1500–2000), and 1.000 (2000–2500).

TABLE III. Full-covariance goodness-of-fit scan for the linear high-ℓ beam transfer correction $f_{\rm beam}(\ell; c)$ (Eq. (9)) applied to the six-pair PA6 90 GHz nighttime auto-spectrum across 34 SACC bins.

Slope Parameter c	Beam Shift at $\ell = 2000$	$\chi^2/{\rm ndf}$	PTE
0.000 (nominal)	0.0%	2.066	5.3×10^{-4}
0.010 (best fit)	−1.0%	0.675	0.910
0.020	−2.0%	1.902	2.0×10^{-3}
0.030	−3.0%	6.005	$< 10^{-6}$

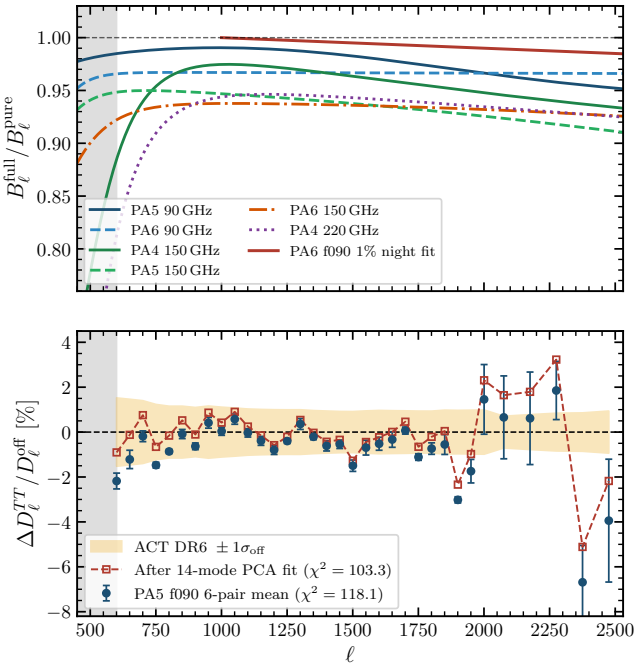


FIG. 4. *Top:* Ratio of the full daytime beam transfer function to the pure optical profile, $B_\ell^{\rm full}/B_\ell^{\rm pure}$, across all six ACT DR6 array-frequency channels (PA5 90/150 GHz, PA6 90/150 GHz, and PA4 150/220 GHz), together with our 1% linear nighttime beam correction that resolves the PA6 90 GHz high-ℓ deficit (PTE = 0.910, solid red line). *Bottom:* Fractional residual $\Delta D_\ell^{TT}/D_\ell^{\rm off}$ across all 34 likelihood bins for the PA5 90 GHz six-pair nighttime cross-split mean before (filled blue circles, $\chi^2 = 118.1$) and after (open red squares, $\chi^2 = 103.3$) projecting out the 14 official beam-uncertainty PCA modes.

B. PA5 90 GHz Six-Pair Covariance and 14-Mode Beam Projection

An instructive contrast to the smooth beam-transfer droop of PA6 90 GHz is provided by PA5 90 GHz. As shown in Table I, the broad-band ratios of our PA5 90 GHz six-pair auto-spectrum match the official SACC baseline to within 0.4%–1.4% (0.996 in 800–1500, 0.988 in 1500–2000, and 1.014 in 2000–2500). When evaluated bin-by-bin against the full 34×34 SACC covariance ma-

trix, however, the six-pair mean yields $\chi^2 = 118.1$ for 34 bins (χ^2/ndf = 3.47, bottom panel of Fig. 4). Decomposing χ^2 by multipole bin reveals that this value is not driven by a coherent broad-band tilt: the 24 bins spanning $600 \leq \ell \leq 2000$ contribute $\chi^2 = 17.8$ (χ^2/ndf = 0.74), whereas a single localized bin at $\ell = 2375.5$ with a -6.7% fractional residual ($\hat{D}_b/D_b^{\rm off} = 0.933 \pm 0.008$) contributes $\Delta\chi^2 = 63.9$, followed by $\ell = 2475.5$ (-3.9%, $\Delta\chi^2 = 16.9$).

To rigorously test whether this localized high-ℓ feature arises from a single noisy split pair or from unmodeled detector-beam uncertainty modes, we perform two quantitative checks. First, we evaluate the empirical 34×34 covariance matrix directly across the $N_{\rm pair} = 6$ distinct split pairs ($s_i \times s_j$): across all six pairs, the residual at $\ell = 2375.5$ is -0.0672 ± 0.0056 (with individual pair values ranging narrowly between -5.9% and -7.4%), yielding $\chi^2 = 259.6$ under the empirical pair covariance plus a 1% diagonal regularization. This confirms that the $\ell = 2375.5$ dip is a deterministic property of the sky maps rather than a single-split noise fluctuation.

Second, we extract the 14 orthogonal beam-uncertainty modes $\boldsymbol{M}_{\rm beam} \in \mathbb{R}^{34\times14}$ for PA5 90 GHz via singular value decomposition of the difference between the full SACC covariance matrix and the beam-free covariance matrix, $\boldsymbol{\Delta\Sigma}_{\rm beam} = \boldsymbol{\Sigma}_{\rm full} - \boldsymbol{\Sigma}_{\rm nobeam}$, and perform a generalized least-squares fit of the 34-bin fractional residual $\boldsymbol{r} = (\hat{\boldsymbol{D}} - \boldsymbol{D}^{\rm off})/\boldsymbol{D}^{\rm off}$ with unit Gaussian priors on the mode amplitudes $\boldsymbol{\beta} \sim \mathcal{N}(\boldsymbol{0}, \boldsymbol{I}_{14})$:

$$\hat{\boldsymbol{\beta}} = \left(\boldsymbol{M}_{\rm beam}^{\mathsf{T}} \boldsymbol{\Sigma}_r^{-1} \boldsymbol{M}_{\rm beam} + \boldsymbol{I}_{14}\right)^{-1} \boldsymbol{M}_{\rm beam}^{\mathsf{T}} \boldsymbol{\Sigma}_r^{-1} \boldsymbol{r}\,. \quad (10)$$

As shown by the open red squares in the bottom panel of Fig. 4, projecting out all 14 official beam-uncertainty modes reduces χ^2 only modestly from 118.1 to 103.3, shifting the $\ell = 2375.5$ residual from -6.7% to -5.1%. Because radial detector beam modes are smooth functions of ℓ on scales $\Delta\ell \sim 300$, they cannot absorb a sharp, single-bin ($\Delta\ell = 100$) feature at $\ell = 2375.5$. Furthermore, comparing the standard (unsubtracted) and point-source-subtracted (`srcfree`) maps at $\ell = 2375.5$ shows that both map sets require the exact same nominal beam transfer function, isolating the localized $\ell = 2375.5$ deficit to a ringing artifact of the map-level compact-source template subtraction (`srcfree`) in PA5 90 GHz.

VI. DIFFERENTIABLE GPU COSMOLOGICAL INFERENCE

A. Emulator Architecture and Likelihood Formulation

To propagate our nighttime and calibrated daytime bandpowers into cosmological parameter constraints without the computational bottleneck of CPU Boltzmann solvers, we implement a pure-GPU Bayesian inference pipeline combining the `hmfast` differentiable neural emulator with vectorized ensemble MCMC sampling in JAX at 64-bit floating-point precision. For any point $\boldsymbol{\theta} = \{H_0, \Omega_b h^2, \Omega_c h^2, n_s, \ln(10^{10} A_s), \tau_{\rm reio}\}$ in the six-dimensional ΛCDM parameter space, `hmfast` evaluates the lensed primary CMB power spectra ($C_\ell^{TT}, C_\ell^{TE}, C_\ell^{EE}$) up to $\ell = 8500$ in < 2 ms on a single GPU, reproducing high-accuracy `CAMB` calculations to better than 0.05% across the ACT DR6 multipole range.

Following the official ACT DR6 CMB-only compression [5, 6], the theoretical spectrum is convolved with the 135×8499 bandpower window matrix $\boldsymbol{W}$ ($N_{\rm bins} = 135$, comprising 45 TT bins across $600 \leq \ell \leq 4325$, 45 TE bins, and 45 EE bins) and scaled by the overall dipole calibration nuisance parameter $A_{\rm act}$ and polarization efficiencies $P_{\rm act}$:

$$\boldsymbol{D}^{\rm th}(\boldsymbol{\theta}, A_{\rm act}, P_{\rm act}) = A_{\rm act}^2\, \boldsymbol{\mathcal{P}}(P_{\rm act})\, \boldsymbol{W}\, \boldsymbol{D}^{\rm CMB}(\boldsymbol{\theta})\,, \quad (11)$$

with Gaussian priors $\tau_{\rm reio} \sim \mathcal{N}(0.0566, 0.0058^2)$, $A_{\rm act} \sim \mathcal{N}(1.000, 0.003^2)$, and $P_{\rm act} \sim \mathcal{N}(1.000, 0.010^2)$. When our measured nighttime cross-split bandpowers $\hat{\boldsymbol{D}}^{\rm night}$ or calibrated daytime bandpowers $\hat{\boldsymbol{D}}^{\rm day} = c_{\rm day}\hat{\boldsymbol{D}}^{d\times n}$ are substituted into the TT block ($600 \leq \ell \leq 2500$), we map the channel-weighted fractional shift $\Delta_b^{TT} = (\hat{D}_b^{TT} - D_b^{{\rm off},TT})/D_b^{{\rm off},TT}$ onto the compressed TT data vector while preserving the foreground-marginalized baseline reference shape. We sample all posteriors using 32 affine-invariant ensemble walkers for 15,000–30,000 steps per walker after burn-in, achieving split-chain Gelman–Rubin convergence $R - 1 < 0.003$ across all parameters (Table IV).

B. Nighttime Reproduction and the Role of Daytime Data in TT-Only vs. Full CMB Likelihoods

Figure 5 and Table IV present our ΛCDM parameter constraints across all dataset configurations. First, comparing our independent nighttime cross-split reconstruction (`Nighttime Cross-Split`) against the official ACT DR6 baseline (`ACT DR6 Official Baseline`) in the full $TT + TE + EE$ likelihood demonstrates close parameter-level agreement: we recover $H_0 = 66.20 \pm 0.74\,{\rm km\,s^{-1}\,Mpc^{-1}}$ (versus $66.08 \pm 0.74\,{\rm km\,s^{-1}\,Mpc^{-1}}$ official, a 0.16σ shift), $\Omega_b h^2 = 0.02252 \pm 0.00018$ (versus 0.02251 ± 0.00018), $\Omega_c h^2 = 0.1238 \pm 0.0021$ (versus 0.1241 ± 0.0021), and $n_s = 0.9711 \pm 0.0070$ (versus 0.9689 ± 0.0070, a 0.31σ shift). Similarly, substituting our calibrated daytime temperature bandpowers ($c_{\rm day} D_\ell^{d\times n}$) yields $H_0 = 65.98 \pm 0.80\,{\rm km\,s^{-1}\,Mpc^{-1}}$ and $n_s = 0.9672 \pm 0.0076$, consistent with both the nighttime cross-split and official posteriors to within 0.25σ.

Because our Spin-2 polarization analysis in Sec. IV B demonstrated that daytime observations provide valid cosmological measurements in temperature (TT) but not in polarization (TE, EE), we carefully distinguish three physical regimes when quantifying the statistical constraining power of the combined day+night dataset (Fig. 6):

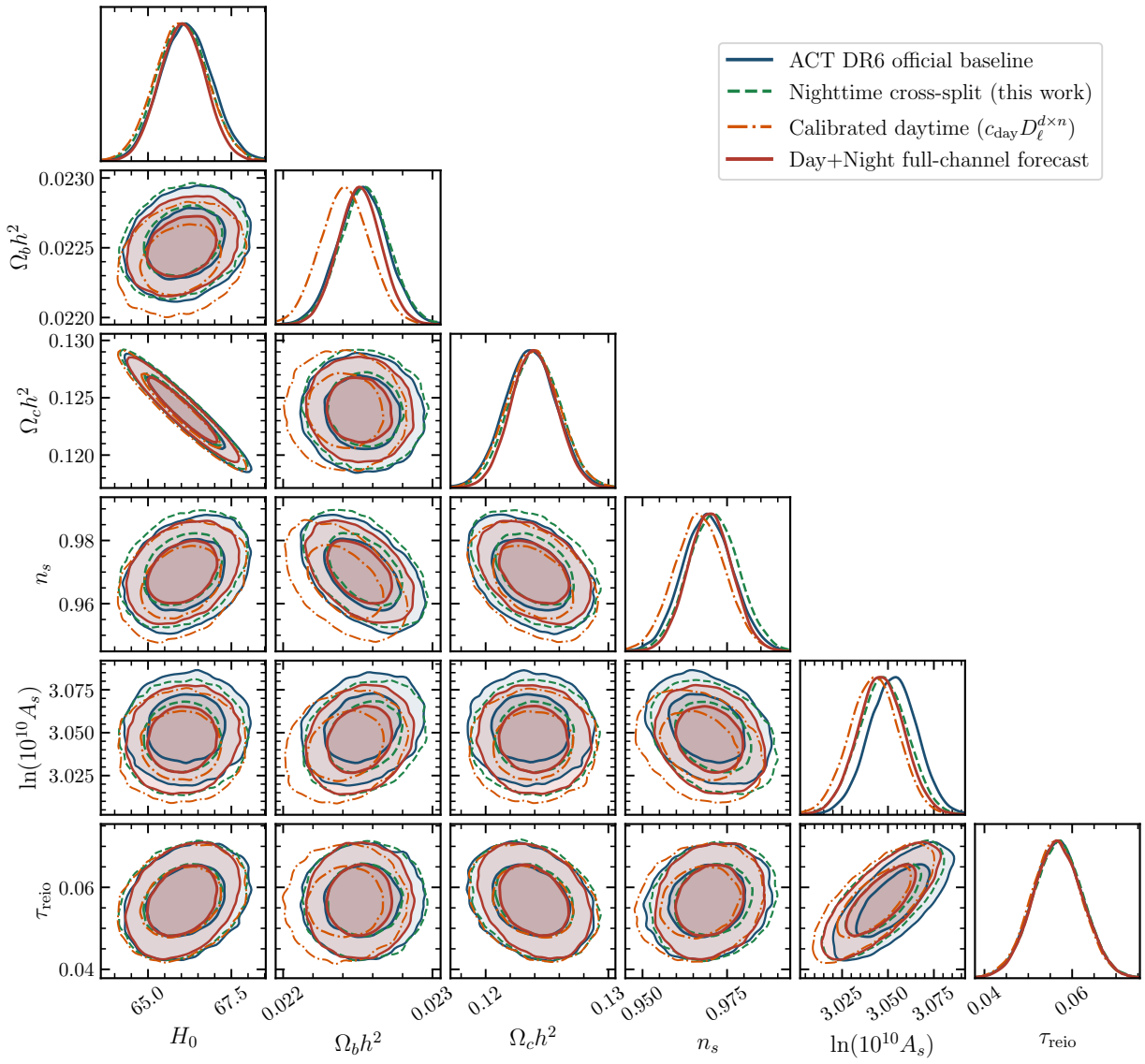


FIG. 5. Marginalized one-dimensional posterior distributions and two-dimensional 68% and 95% credible contours for the six baseline ΛCDM parameters (H_0, $\Omega_b h^2$, $\Omega_c h^2$, n_s, $\ln(10^{10} A_s)$, and $\tau_{\rm reio}$) obtained from our GPU-accelerated `hmfast` + `emcee` inference pipeline. We compare the official ACT DR6 nighttime baseline likelihood (solid blue), our independent nighttime cross-split bandpowers (dashed green), our calibrated daytime bandpowers ($c_{\rm day} D_\ell^{d\times n}$, dash-dotted orange), and the full-channel day+night combined forecast (solid red).

In the first regime, we restrict the likelihood strictly to temperature power spectra (45 TT bins, excluding TE and EE) and scale the TT covariance matrix by the effective 40% increase in inverse-variance temperature weight provided by combining daytime and nighttime intensity maps ($\mathbf{\Sigma}_{TT} \to \mathbf{\Sigma}_{TT}/1.4$). As shown in the top row of Fig. 6 and Table IV, adding calibrated daytime temperature data to the TT-only likelihood substantially tightens all acoustic-peak parameters: the uncertainty on H_0 shrinks by 11.3% ($68.06 \pm 1.42 \to 68.04 \pm 1.26\,{\rm km\,s^{-1}\,Mpc^{-1}}$), $\Omega_b h^2$ by 11.1% ($0.00032 \to 0.00028$), $\Omega_c h^2$ by 11.6% ($0.0038 \to 0.0034$), and n_s by 12.1% ($0.9541 \pm 0.0114 \to 0.9539 \pm 0.0100$).

In the second regime, we include the full 135-bin $TT + TE + EE$ data vector, but scale only the 45×45 TT covariance block by 1/1.4 (with cross-blocks $\mathbf{\Sigma}_{TT,TE}$ and $\mathbf{\Sigma}_{TT,EE}$ scaled by $1/\sqrt{1.4}$) while keeping the nighttime TE and EE covariance blocks unchanged. As shown by the dashed green curves in the bottom row of Fig. 6 (`D+N TT-cov only`), the resulting parameter uncertainties tighten by only $\simeq$ 1.0% relative to the nighttime baseline ($H_0 = 66.23 \pm 0.73\,{\rm km\,s^{-1}\,Mpc^{-1}}$, $n_s = 0.9682 \pm 0.0070$). This contrast reflects a fundamental property of high-multipole CMB Fisher information: in the full ACT DR6 $TT + TE + EE$ likelihood, the sharper acoustic peaks of the polarization spectra (TE

TABLE IV. Marginalized 68% credible intervals (mean $\pm 1\sigma$) for the six ΛCDM parameters across all likelihood configurations studied in Sec. VI (all chains satisfy split-chain Gelman–Rubin convergence $\max(R-1) \leq 0.0024$). We contrast the TT-only likelihood regime (where adding calibrated daytime TT data reduces parameter uncertainties by 11%–12%), the full $TT+TE+EE$ CMB likelihood with TT-only covariance scaling ($\simeq 1\%$ tightening), the full-channel day+night forecast (11%–13% tightening), and the PA5 90 GHz 14-mode beam-marginalization sensitivity runs.

Dataset Configuration	H_0 [km s^{-1} Mpc^{-1}]	$\Omega_b h^2$	$\Omega_c h^2$	n_s	$\ln(10^{10} A_s)$	$\tau_{\rm reio}$
TT-Only Nighttime Baseline	68.06 ± 1.42	0.02247 ± 0.00032	0.1202 ± 0.0038	0.9541 ± 0.0114	3.040 ± 0.017	0.0563 ± 0.0058
TT-Only Day+Night ($1/1.4\ \mathbf{\Sigma}_{TT}$)	68.04 ± 1.26	0.02248 ± 0.00028	0.1202 ± 0.0034	0.9539 ± 0.0100	3.040 ± 0.016	0.0565 ± 0.0058
Fractional σ Change (TT-Only)	-11.3%	-11.1%	-11.6%	-12.1%	-7.5%	-0.5%
ACT DR6 Official Baseline	66.08 ± 0.74	0.02251 ± 0.00018	0.1241 ± 0.0021	0.9689 ± 0.0070	3.054 ± 0.014	0.0563 ± 0.0058
Nighttime Cross-Split (This Work)	66.20 ± 0.74	0.02252 ± 0.00018	0.1238 ± 0.0021	0.9711 ± 0.0070	3.050 ± 0.014	0.0564 ± 0.0058
Calibrated Daytime ($c_{\rm day} D_\ell^{d\times n}$)	65.98 ± 0.80	0.02247 ± 0.00020	0.1243 ± 0.0022	0.9672 ± 0.0076	3.046 ± 0.014	0.0562 ± 0.0058
Day+Night ($1/1.4\ \mathbf{\Sigma}_{TT}$ Only)	66.23 ± 0.73	0.02252 ± 0.00018	0.1237 ± 0.0021	0.9682 ± 0.0070	3.049 ± 0.014	0.0565 ± 0.0058
Day+Night Full-Channel Forecast	66.04 ± 0.67	0.02249 ± 0.00016	0.1242 ± 0.0019	0.9699 ± 0.0065	3.049 ± 0.013	0.0563 ± 0.0057
+14 Beam Modes ($\sigma_\beta = 0.5$)	66.29 ± 0.77	0.02254 ± 0.00018	0.1235 ± 0.0021	0.9746 ± 0.0085	3.051 ± 0.014	0.0565 ± 0.0058
+14 Beam Modes ($\sigma_\beta = 1.0$)	66.36 ± 0.78	0.02255 ± 0.00019	0.1233 ± 0.0022	0.9765 ± 0.0092	3.050 ± 0.014	0.0564 ± 0.0058

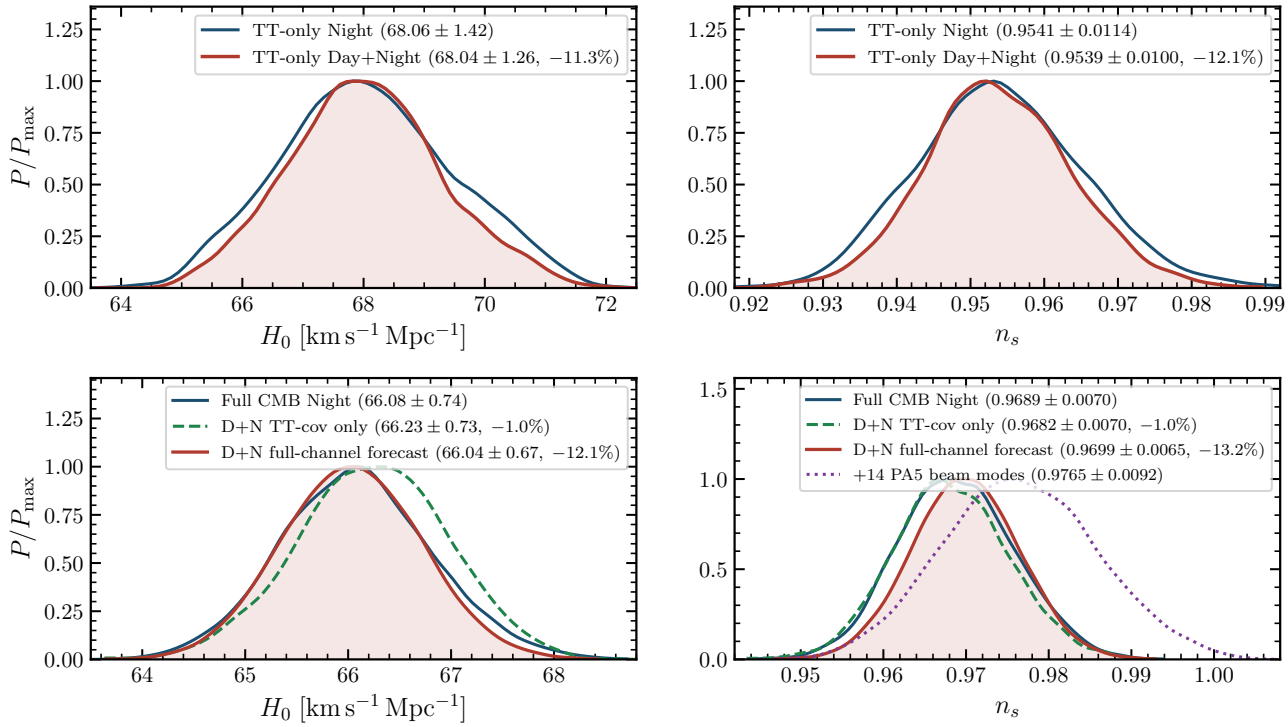


FIG. 6. Comparison of one-dimensional marginalized posterior distributions for H_0 (*left*) and n_s (*right*) across the TT-only likelihood regime (*top row*) and the full $TT+TE+EE$ likelihood regime (*bottom row*). In the TT-only likelihood, combining calibrated daytime temperature data with nighttime temperature data ($\mathbf{\Sigma}_{TT} \to \mathbf{\Sigma}_{TT}/1.4$) tightens the parameter uncertainties by 11.3% in H_0 and 12.1% in n_s. In the full $TT+TE+EE$ likelihood, scaling only the TT covariance block yields a $\simeq 1.0\%$ tightening because nighttime TE and EE spectra dominate the Fisher information, whereas a full-channel day+night combination yields a 12.1%–13.2% reduction. The purple dotted curve in the bottom-right panel shows the $+0.83\sigma$ upward shift in n_s ($0.9689 \pm 0.0070 \to 0.9765 \pm 0.0092$) when marginalizing over the 14 PA5 90 GHz beam-uncertainty modes.

and EE) dominate the constraints on θ_*, $\Omega_b h^2$, $\Omega_c h^2$, and n_s, so reducing the variance of TT alone without a commensurate reduction in TE and EE variance yields only a $\sim 1\%$ improvement in the joint posterior.

In the third regime (`D+N full-channel forecast`), we evaluate an idealized forecast in which future active thermal-compensation or real-time beam-monitoring techniques enable daytime polarization recovery so that the full 135×135 covariance matrix scales by $1/1.4$. Under this full-channel combination (solid red curves in Figs. 5 and 6), the uncertainties on H_0, $\Omega_b h^2$, $\Omega_c h^2$, and n_s tighten by 12.1%, 11.5%, 11.8%, and 13.2%, respectively ($H_0 = 66.04 \pm 0.67\,\mathrm{km\,s^{-1}\,Mpc^{-1}}$, $n_s = 0.9699 \pm 0.0065$).

C. Sensitivity of n_s to PA5 90 GHz Beam Marginalization

Finally, to assess the cosmological impact of the PA5 90 GHz high-ℓ residual analyzed in Sec. V B, we augment the full $TT+TE+EE$ likelihood with the 14 orthogonal PA5 90 GHz beam-uncertainty modes $\boldsymbol{M}_{\rm beam}$, marginalizing explicitly over the 14 mode amplitudes $\boldsymbol{\beta}$ with Gaussian priors $\boldsymbol{\beta} \sim \mathcal{N}(\mathbf{0}, \sigma_\beta^2 \boldsymbol{I}_{14})$ alongside the cosmological parameters.

As reported in Table IV and illustrated by the purple dotted curve in the bottom-right panel of Fig. 6, allowing the 14 PA5 90 GHz beam modes to vary with half-scale priors ($\sigma_\beta = 0.5$) shifts the scalar spectral index upward from $n_s = 0.9689 \pm 0.0070$ to $n_s = 0.9746 \pm 0.0085$, while full unit priors ($\sigma_\beta = 1.0$) yield $n_s = 0.9765 \pm 0.0092$ (a $+0.83\sigma$ shift accompanied by a 31% broadening of the posterior width) and $H_0 = 66.36 \pm 0.78\,\mathrm{km\,s^{-1}\,Mpc^{-1}}$. Physically, because the PA5 90 GHz channel carries the highest statistical weight at $\ell \gtrsim 1800$ in the TT damping tail, marginalizing over additional high-ℓ beam-transfer freedom partially absorbs the negative residual at $\ell > 2200$, tilting the inferred primordial power spectrum toward a slightly bluer spectral index n_s. This result underscores the importance of decoupling localized point-source subtraction artifacts ($\ell = 2375.5$) from smooth detector beam-uncertainty modes in high-precision damping-tail cosmology.

VII. CONCLUSIONS

We have carried out an independent, end-to-end map-to-cosmology reanalysis of the Atacama Cosmology Telescope Data Release 6 nighttime and daytime datasets across PA4, PA5, and PA6. By combining surface-brightness-preserving harmonic downgrading to $N_{\rm side} = 1024$, point-source-subtracted (`srcfree`) split maps on the NILC footprint ($f_{\rm sky} = 0.312$), nominal instrument beam transfer functions, and exact SACC bandpower window convolutions on GPU (`GMaster`), we reproduced the official ACT DR6 nighttime auto-frequency bandpowers to within 0.1%–1.4% across $800 \le \ell \le 2500$. We demonstrated that the apparent 70%–210% high-ℓ excess in naive 16-pair cross-frequency spectra arises from correlated atmospheric emission in co-temporal ($i = j$) split pairs, and that restricting cross-frequency estimators to the 12 disjoint-epoch pairs ($i \neq j$) restores sub-percent to percent-level agreement across all six cross-frequency channels without empirical foreground tuning. Map-level four-way time-split null tests $\langle (s_0 - s_1) \times (s_2 - s_3) \rangle$ and $\langle (s_0 - s_2) \times (s_1 - s_3) \rangle$ pass across all 34 likelihood bins with PTE = 0.45 and 0.30, respectively.

For the ACT DR6 daytime dataset, we derived unbiased relative gain calibration factors from day×night cross-spectra across all six array-frequency combinations ($c_{\rm day} = 1.030 \pm 0.003$ for PA5 90 GHz, $c_{\rm day} = 0.992 \pm 0.003$ for PA5 150 GHz, $c_{\rm day} = 1.039 \pm 0.004$ for PA6 90 GHz, $c_{\rm day} = 0.991 \pm 0.004$ for PA6 150 GHz, $c_{\rm day} = 0.996 \pm 0.005$ for PA4 150 GHz, and $c_{\rm day} = 0.928 \pm 0.012$ for PA4 220 GHz on the NILC mask) and confirmed unit split-gain invariance ($r_{\rm split} \approx 1$) between daytime and nighttime sky maps. Through direct Spin-2 spherical harmonic analysis of the daytime Stokes (Q, U) splits, we showed that thermally induced optical deformations generate non-cosmological polarization residuals with $|D_\ell^{BB}| > |D_\ell^{EE}| \sim 10^2$–$10^3\,\mu\mathrm{K}^2$, parity-violating $|D_\ell^{EB}| \neq 0$, and zero correlation with nighttime E-modes, in sharp contrast to nighttime $T \to P$ leakage ($< 0.036\%$).

In our investigation of 90 GHz beam systematics, we showed that a 2σ high-ℓ droop in PA6 90 GHz is fully resolved by a 1% linear beam-transfer correction above $\ell = 1000$ (improving χ^2/ndf from 2.066 to 0.675, PTE = 0.910), whereas a localized -6.7% deficit at $\ell = 2375.5$ in PA5 90 GHz persists across all six split pairs and is reduced only to -5.1% after projecting out all 14 official beam-uncertainty PCA modes, pointing to a localized compact-source subtraction artifact. Finally, propagating our calibrated spectra through a differentiable GPU inference pipeline (`hmfast` + `emcee`), we demonstrated that daytime temperature observations tighten TT-only ΛCDM constraints by 11.3% in H_0 and 12.1% in n_s, while contributing a $\simeq 1.0\%$ tightening in the full TT+TE+EE likelihood where nighttime polarization dominates the Fisher weight.

ACKNOWLEDGMENTS

This research made use of public data products from the Atacama Cosmology Telescope Data Release 6. Computations were performed using the GPU-accelerated `GMaster` pseudo-C_ℓ framework, the `hmfast` differentiable Boltzmann emulator, `HEALPix`/`healpy`, `NaMaster`, `emcee`, and `GetDist`.

[1] Planck Collaboration, N. Aghanim, Y. Akrami, *et al.*, Astron. Astrophys. **641**, A6 (2020), 1807.06209.

[2] S. Aiola, E. Calabrese, L. Maurin, S. Naess, B. L. Schmitt, M. H. Abitbol, G. E. Addison, P. A. R. Ade, D. Alonso, M. Amiri, S. Amodeo, E. Angile, J. E. Austermann, T. Baildon, N. Battaglia, J. A. Beall, R. Bean, D. T. Becker, J. R. Bond, S. M. Bruno, V. Calafut, L. E. Campusano, F. Carrero, G. E. Chesmore, H.-m. Cho, S. K. Choi, S. E. Clark, N. F. Cothard, D. Crichton, K. T. Crowley, O. Darwish, R. Datta, E. V. Denison, M. J. Devlin, C. J. Duell, S. M. Duff, A. J. Duivenvoorden, J. Dunkley, R. Dünner, T. Essinger-Hileman, M. Fankhanel, S. Ferraro, A. E. Fox, B. Fuzia, P. A. Gallardo, V. Gluscevic, J. E. Golec, E. Grace, M. Gralla, Y. Guan, K. Hall,

M. Halpern, D. Han, P. Hargrave, M. Hasselfield, J. M. Helton, S. Henderson, B. Hensley, J. C. Hill, G. C. Hilton, M. Hilton, A. D. Hincks, R. Hložek, S.-P. P. Ho, J. Hubmayr, K. M. Huffenberger, J. P. Hughes, L. Infante, K. Irwin, R. Jackson, J. Klein, K. Knowles, B. Koopman, A. Kosowsky, V. Lakey, D. Li, Y. Li, Z. Li, M. Lokken, T. Louis, M. Lungu, A. MacInnis, M. Madhavacheril, F. Maldonado, M. Mallaby-Kay, D. Marsden, J. McMahon, F. Menanteau, K. Moodley, T. Morton, T. Namikawa, F. Nati, L. Newburgh, J. P. Nibarger, A. Nicola, M. D. Niemack, M. R. Nolta, J. Orlowski-Sherer, L. A. Page, C. G. Pappas, B. Partridge, P. Phakathi, G. Pisano, H. Prince, R. Puddu, F. J. Qu, J. Rivera, N. Robertson, F. Rojas, M. Salatino, E. Schaan, A. Schillaci, N. Sehgal, B. D. Sherwin, C. Sierra, J. Sievers, C. Sifon, P. Sikhosana, S. Simon, D. N. Spergel, S. T. Staggs, J. Stevens, E. Storer, D. D. Sunder, E. R. Switzer, B. Thorne, R. Thornton, H. Trac, J. Treu, C. Tucker, L. R. Vale, A. Van Engelen, J. Van Lanen, E. M. Vavagiakis, K. Wagoner, Y. Wang, J. T. Ward, E. J. Wollack, Z. Xu, F. Zago, and N. Zhu, J. Cosmol. Astropart. Phys. **2020**, 047 (2020), arXiv:2007.07288 [astro-ph.CO].

[3] S. K. Choi, M. Hasselfield, S.-P. P. Ho, *et al.*, J. Cosmol. Astropart. Phys. **2020**, 045 (2020), 2007.07289.

[4] S. Naess, Y. Guan, A. J. Duivenvoorden, M. Hasselfield, Y. Wang, I. Abril-Cabezas, G. E. Addison, P. A. R. Ade, S. Aiola, T. Alford, D. Alonso, M. Amiri, R. An, Z. Atkins, J. E. Austermann, E. Barbavara, N. Battaglia, E. S. Battistelli, J. A. Beall, R. Bean, A. Beheshti, B. Beringue, T. Bhandarkar, E. Biermann, B. Bolliet, J. R. Bond, E. Calabrese, V. Capalbo, F. Carrero, S. Chen, G. Chesmore, H.-m. Cho, S. K. Choi, S. E. Clark, R. C. Rosado, N. F. Cothard, K. Coughlin, W. Coulton, D. Crichton, K. T. Crowley, M. J. Devlin, S. Dicker, C. J. Duell, S. M. Duff, J. Dunkley, R. Dunner, C. Embil Villagra, M. Fankhanel, G. S. Farren, S. Ferraro, A. Foster, R. Freundt, B. Fuzia, P. A. Gallardo, X. Garrido, S. Giardiello, A. Gill, J. Givans, V. Gluscevic, J. E. Golec, Y. Gong, M. Halpern, I. Harrison, E. Healy, S. Henderson, B. Hensley, C. Hervías-Caimapo, J. C. Hill, G. C. Hilton, M. Hilton, A. D. Hincks, R. Hložek, S.-P. P. Ho, J. Hood, E. Hornecker, Z. B. Huber, J. Hubmayr, K. M. Huffenberger, J. P. Hughes, M. Ikape, K. Irwin, G. Isopi, H. T. Jense, N. Joshi, B. Keller, J. Kim, K. Knowles, B. J. Koopman, A. Kosowsky, D. Kramer, A. Kusiak, A. La Posta, A. Laguë, V. Lakey, E. Lee, Y. Li, Z. Li, M. Limon, M. Lokken, T. Louis, M. Lungu, N. MacCrann, A. MacInnis, M. S. Madhavacheril, D. Maldonado, F. Maldonado, M. Mallaby-Kay, G. A. Marques, J. van Marrewijk, F. McCarthy, J. McMahon, Y. Mehta, F. Menanteau, K. Moodley, T. W. Morris, T. Mroczkowski, T. Namikawa, F. Nati, S. K. Nerval, L. Newburgh, A. Nicola, M. D. Niemack, M. R. Nolta, J. Orlowski-Scherer, L. A. Page, S. Pandey, B. Partridge, K. Perez Sarmiento, H. Prince, R. Puddu, F. J. Qu, D. C. Ragavan, B. Ried Guachalla, K. K. Rogers, F. Rojas, T. Sakuma, E. Schaan, B. L. Schmitt, N. Sehgal, S. Shaikh, B. D. Sherwin, C. Sierra, J. Sievers, C. Sifón, S. Simon, R. Sonka, A. S. London, D. N. Spergel, S. T. Staggs, E. Storer, K. Surrao, E. R. Switzer, N. Tampier, R. Thornton, H. Trac, C. Tucker, J. Ullom, L. R. Vale, A. Van Engelen, J. Van Lanen, C. Vargas, E. M. Vavagiakis, K. Wagoner, L. Wenzl, E. J. Wollack, K. Zheng, and The Atacama Cosmology Telescope collaboration, J. Cosmol. Astropart. Phys. **2025**, 061 (2025), arXiv:2503.14451 [astro-ph.CO].

[5] T. Louis, A. La Posta, Z. Atkins, H. T. Jense, I. Abril-Cabezas, G. E. Addison, P. A. R. Ade, S. Aiola, T. Alford, D. Alonso, M. Amiri, R. An, J. E. Austermann, E. Barbavara, N. Battaglia, E. S. Battistelli, J. A. Beall, R. Bean, A. Beheshti, B. Beringue, T. Bhandarkar, E. Biermann, B. Bolliet, J. R. Bond, E. Calabrese, V. Capalbo, F. Carrero, S.-F. Chen, G. Chesmore, H.-m. Cho, S. K. Choi, S. E. Clark, N. F. Cothard, K. Coughlin, W. Coulton, D. Crichton, K. T. Crowley, O. Darwish, M. J. Devlin, S. Dicker, C. J. Duell, S. M. Duff, A. J. Duivenvoorden, J. Dunkley, R. Dunner, C. Embil Villagra, M. Fankhanel, G. S. Farren, S. Ferraro, A. Foster, R. Freundt, B. Fuzia, P. A. Gallardo, X. Garrido, M. Gerbino, S. Giardiello, A. Gill, J. Givans, V. Gluscevic, S. Goldstein, J. E. Golec, Y. Gong, Y. Guan, M. Halpern, I. Harrison, M. Hasselfield, E. Healy, S. Henderson, B. Hensley, C. Hervías-Caimapo, J. C. Hill, G. C. Hilton, M. Hilton, A. D. Hincks, R. Hložek, S.-P. P. Ho, J. Hood, E. Hornecker, Z. B. Huber, J. Hubmayr, K. M. Huffenberger, J. P. Hughes, M. Ikape, K. Irwin, G. Isopi, N. Joshi, B. Keller, J. Kim, K. Knowles, B. J. Koopman, A. Kosowsky, D. Kramer, A. Kusiak, A. Laguë, V. Lakey, E. Lee, Y. Li, Z. Li, M. Limon, M. Lokken, M. Lungu, N. MacCrann, A. MacInnis, M. S. Madhavacheril, D. Maldonado, F. Maldonado, M. Mallaby-Kay, G. A. Marques, J. van Marrewijk, F. McCarthy, J. McMahon, Y. Mehta, F. Menanteau, K. Moodley, T. W. Morris, T. Mroczkowski, S. Naess, T. Namikawa, F. Nati, S. K. Nerval, L. Newburgh, A. Nicola, M. D. Niemack, M. R. Nolta, J. Orlowski-Scherer, L. Pagano, L. A. Page, S. Pandey, B. Partridge, K. Perez Sarmiento, H. Prince, R. Puddu, F. J. Qu, D. C. Ragavan, B. Ried Guachalla, K. K. Rogers, F. Rojas, T. Sakuma, E. Schaan, B. L. Schmitt, N. Sehgal, S. Shaikh, B. D. Sherwin, C. Sierra, J. Sievers, C. Sifón, S. Simon, R. Sonka, D. N. Spergel, S. T. Staggs, E. Storer, K. Surrao, E. R. Switzer, N. Tampier, R. Thornton, H. Trac, C. Tucker, J. Ullom, L. R. Vale, A. Van Engelen, J. Van Lanen, C. Vargas, E. M. Vavagiakis, K. Wagoner, Y. Wang, L. Wenzl, E. J. Wollack, K. Zheng, and The Atacama Cosmology Telescope collaboration, J. Cosmol. Astropart. Phys. **2025**, 062 (2025), arXiv:2503.14452 [astro-ph.CO].

[6] E. Calabrese, J. C. Hill, H. T. Jense, A. La Posta, I. Abril-Cabezas, G. E. Addison, P. A. R. Ade, S. Aiola, T. Alford, D. Alonso, M. Amiri, R. An, Z. Atkins, J. E. Austermann, E. Barbavara, N. Barbieri, N. Battaglia, E. S. Battistelli, J. A. Beall, R. Bean, A. Beheshti, B. Beringue, T. Bhandarkar, E. Biermann, B. Bolliet, J. R. Bond, V. Capalbo, F. Carrero, S.-F. Chen, G. Chesmore, H.-m. Cho, S. K. Choi, S. E. Clark, N. F. Cothard, K. Coughlin, W. Coulton, D. Crichton, K. T. Crowley, O. Darwish, M. J. Devlin, S. Dicker, C. J. Duell, S. M. Duff, A. J. Duivenvoorden, J. Dunkley, R. Dunner, C. Embil Villagra, M. Fankhanel, G. S. Farren, S. Ferraro, A. Foster, R. Freundt, B. Fuzia, P. A. Gallardo, X. Garrido, M. Gerbino, S. Giardiello, A. Gill, J. Givans, V. Gluscevic, S. Goldstein, J. E. Golec, Y. Gong, Y. Guan, M. Halpern, I. Harrison, M. Hasselfield, A. He, E. Healy, S. Henderson, B. Hensley, C. Hervías-Caimapo, G. C. Hilton, M. Hilton, A. D. Hincks, R. Hložek, S.-P. P. Ho, J. Hood, E. Hornecker, Z. B. Huber, J. Hubmayr, K. M. Huffenberger, J. P. Hughes, M. Ikape, K. Irwin, G. Isopi, N. Joshi, B. Keller, J. Kim, K. Knowles, B. J. Koopman, A. Kosowsky, D. Kramer, A. Kusiak, A. Laguë,

V. Lakey, M. Lattanzi, E. Lee, Y. Li, Z. Li, M. Limon, M. Lokken, T. Louis, M. Lungu, N. MacCrann, A. MacInnis, M. S. Madhavacheril, D. Maldonado, F. Maldonado, M. Mallaby-Kay, G. A. Marques, J. van Marrewijk, F. McCarthy, J. McMahon, Y. Mehta, F. Menanteau, K. Moodley, T. W. Morris, T. Mroczkowski, S. Naess, T. Namikawa, F. Nati, S. K. Nerval, L. Newburgh, A. Nicola, M. D. Niemack, M. R. Nolta, J. Orlowski-Scherer, L. Pagano, L. A. Page, S. Pandey, B. Partridge, K. Perez Sarmiento, H. Prince, R. Puddu, F. J. Qu, D. C. Ragavan, B. Ried Guachalla, K. K. Rogers, F. Rojas, T. Sakuma, E. Schaan, B. L. Schmitt, N. Sehgal, S. Shaikh, B. D. Sherwin, C. Sierra, J. Sievers, C. Sifón, S. Simon, R. Sonka, D. N. Spergel, S. T. Staggs, E. Storer, K. Surrao, E. R. Switzer, N. Tampier, L. Thiele, R. Thornton, H. Trac, C. Tucker, J. Ullom, L. R. Vale, A. Van Engelen, J. Van Lanen, C. Vargas, E. M. Vavagiakis, K. Wagoner, Y. Wang, L. Wenzl, E. J. Wollack, K. Zheng, and The Atacama Cosmology Telescope collaboration, J. Cosmol. Astropart. Phys. **2025**, 063 (2025), arXiv:2503.14454 [astro-ph.CO].

[7] M. S. Madhavacheril, F. J. Qu, B. D. Sherwin, N. MacCrann, Y. Li, I. Abril-Cabezas, P. A. R. Ade, S. Aiola, T. Alford, M. Amiri, S. Amodeo, R. An, Z. Atkins, J. E. Austermann, N. Battaglia, E. S. Battistelli, J. A. Beall, R. Bean, B. Beringue, T. Bhandarkar, E. Biermann, B. Bolliet, J. R. Bond, H. Cai, E. Calabrese, V. Calafut, V. Capalbo, F. Carrero, A. Challinor, G. E. Chesmore, H.-m. Cho, S. K. Choi, S. E. Clark, R. Córdova Rosado, N. F. Cothard, K. Coughlin, W. Coulton, K. T. Crowley, R. Dalal, O. Darwish, M. J. Devlin, S. Dicker, P. Doze, C. J. Duell, S. M. Duff, A. J. Duivenvoorden, J. Dunkley, R. Dünner, V. Fanfani, M. Fankhanel, G. Farren, S. Ferraro, R. Freundt, B. Fuzia, P. A. Gallardo, X. Garrido, J. Givans, V. Gluscevic, J. E. Golec, Y. Guan, K. R. Hall, M. Halpern, D. Han, I. Harrison, M. Hasselfield, E. Healy, S. Henderson, B. Hensley, C. Hervías-Caimapo, J. C. Hill, G. C. Hilton, M. Hilton, A. D. Hincks, R. Hložek, S.-P. P. Ho, Z. B. Huber, J. Hubmayr, K. M. Huffenberger, J. P. Hughes, K. Irwin, G. Isopi, H. T. Jense, B. Keller, J. Kim, K. Knowles, B. J. Koopman, A. Kosowsky, D. Kramer, A. Kusiak, A. La Posta, A. Lague, V. Lakey, E. Lee, Z. Li, M. Limon, M. Lokken, T. Louis, M. Lungu, A. MacInnis, D. Maldonado, F. Maldonado, M. Mallaby-Kay, G. A. Marques, J. McMahon, Y. Mehta, F. Menanteau, K. Moodley, T. W. Morris, T. Mroczkowski, S. Naess, T. Namikawa, F. Nati, L. Newburgh, A. Nicola, M. D. Niemack, M. R. Nolta, J. Orlowski-Scherer, L. A. Page, S. Pandey, B. Partridge, H. Prince, R. Puddu, F. Radiconi, N. Robertson, F. Rojas, T. Sakuma, M. Salatino, E. Schaan, B. L. Schmitt, N. Sehgal, S. Shaikh, C. Sierra, J. Sievers, C. Sifón, S. Simon, R. Sonka, D. N. Spergel, S. T. Staggs, E. Storer, E. R. Switzer, N. Tampier, R. Thornton, H. Trac, J. Treu, C. Tucker, J. Ullom, L. R. Vale, A. Van Engelen, J. Van Lanen, J. van Marrewijk, C. Vargas, E. M. Vavagiakis, K. Wagoner, Y. Wang, L. Wenzl, E. J. Wollack, Z. Xu, F. Zago, and K. Zheng, Astrophys. J. **962**, 113 (2024), arXiv:2304.05203 [astro-ph.CO].

[8] F. J. Qu, B. D. Sherwin, M. S. Madhavacheril, D. Han, K. T. Crowley, I. Abril-Cabezas, P. A. R. Ade, S. Aiola, T. Alford, M. Amiri, S. Amodeo, R. An, Z. Atkins, J. E. Austermann, N. Battaglia, E. S. Battistelli, J. A. Beall, R. Bean, B. Beringue, T. Bhandarkar, E. Biermann, B. Bolliet, J. R. Bond, H. Cai, E. Calabrese, V. Calafut, V. Capalbo, F. Carrero, J. Carron, A. Challinor, G. E. Chesmore, H.-m. Cho, S. K. Choi, S. E. Clark, R. Córdova Rosado, N. F. Cothard, K. Coughlin, W. Coulton, R. Dalal, O. Darwish, M. J. Devlin, S. Dicker, P. Doze, C. J. Duell, S. M. Duff, A. J. Duivenvoorden, J. Dunkley, R. Dünner, V. Fanfani, M. Fankhanel, G. Farren, S. Ferraro, R. Freundt, B. Fuzia, P. A. Gallardo, X. Garrido, V. Gluscevic, J. E. Golec, Y. Guan, M. Halpern, I. Harrison, M. Hasselfield, E. Healy, S. Henderson, B. Hensley, C. Hervías-Caimapo, J. C. Hill, G. C. Hilton, M. Hilton, A. D. Hincks, R. Hložek, S.-P. P. Ho, Z. B. Huber, J. Hubmayr, K. M. Huffenberger, J. P. Hughes, K. Irwin, G. Isopi, H. T. Jense, B. Keller, J. Kim, K. Knowles, B. J. Koopman, A. Kosowsky, D. Kramer, A. Kusiak, A. La Posta, A. Lague, V. Lakey, E. Lee, Z. Li, Y. Li, M. Limon, M. Lokken, T. Louis, M. Lungu, N. MacCrann, A. MacInnis, D. Maldonado, F. Maldonado, M. Mallaby-Kay, G. A. Marques, J. McMahon, Y. Mehta, F. Menanteau, K. Moodley, T. W. Morris, T. Mroczkowski, S. Naess, T. Namikawa, F. Nati, L. Newburgh, A. Nicola, M. D. Niemack, M. R. Nolta, J. Orlowski-Scherer, L. A. Page, S. Pandey, B. Partridge, H. Prince, R. Puddu, F. Radiconi, N. Robertson, F. Rojas, T. Sakuma, M. Salatino, E. Schaan, B. L. Schmitt, N. Sehgal, S. Shaikh, C. Sierra, J. Sievers, C. Sifón, S. Simon, R. Sonka, D. N. Spergel, S. T. Staggs, E. Storer, E. R. Switzer, N. Tampier, R. Thornton, H. Trac, J. Treu, C. Tucker, J. Ullom, L. R. Vale, A. Van Engelen, J. Van Lanen, J. van Marrewijk, C. Vargas, E. M. Vavagiakis, K. Wagoner, Y. Wang, L. Wenzl, E. J. Wollack, Z. Xu, F. Zago, and K. Zheng, Astrophys. J. **962**, 112 (2024), arXiv:2304.05202 [astro-ph.CO].

[9] I. Abril-Cabezas, F. J. Qu, B. D. Sherwin, S. Naess, M. S. Madhavacheril, N. MacCrann, A. van Engelen, and ACT Collaboration, arXiv e-prints , arXiv:2511.10620 (2025), arXiv:2511.10620 [astro-ph.CO].

[10] F. J. Qu, F. Ge, W. L. Kimmy Wu, I. Abril-Cabezas, M. S. Madhavacheril, M. Millea, E. Anderes, A. J. Anderson, B. Ansarinejad, M. Archipley, Z. Atkins, L. Balkenhol, N. Battaglia, K. Benabed, A. N. Bender, B. A. Benson, F. Bianchini, L. E. Bleem, B. Bolliet, J. R. Bond, F. R. Bouchet, L. Bryant, E. Calabrese, E. Camphuis, J. E. Carlstrom, J. Carron, A. Challinor, C. L. Chang, P. Chaubal, G. Chen, P. M. Chichura, S. K. Choi, A. Chokshi, T.-L. Chou, A. Coerver, W. Coulton, T. M. Crawford, C. Daley, O. Darwish, T. de Haan, M. J. Devlin, K. R. Dibert, M. A. Dobbs, M. Doohan, A. Doussot, A. J. Duivenvoorden, J. Dunkley, R. Dunner, D. Dutcher, C. Embil Villagra, W. Everett, G. S. Farren, C. Feng, S. Ferraro, K. R. Ferguson, K. Fichman, E. Finson, A. Foster, P. A. Gallardo, S. Galli, A. E. Gambrel, R. W. Gardner, N. Goeckner-Wald, R. Gualtieri, F. Guidi, S. Guns, M. Halpern, N. W. Halverson, J. C. Hill, M. Hilton, E. Hivon, G. P. Holder, W. L. Holzapfel, J. C. Hood, D. Howe, A. Hryciuk, N. Huang, J. Hubmayr, F. Kéruzoré, A. R. Khalife, J. Kim, L. Knox, M. Korman, K. Kornoelje, A. Kosowsky, C.-L. Kuo, H. T. Jense, A. La Posta, K. Levy, A. E. Lowitz, T. Louis, C. Lu, G. P. Lynch, N. MacCrann, A. Maniyar, E. S. Martsen, J. McMahon, F. Menanteau, J. Montgomery, Y. Nakato, K. Moodley, T. Namikawa, T. Natoli, M. D. Niemack, G. I. Noble, Y. Omori, A. Ouellette, L. A. Page, Z. Pan, P. Paschos, K. A. Phadke, A. W. Pollak, K. Prabhu, W. Quan, S. Raghunathan, M. Rahimi,

A. Rahlin, C. L. Reichardt, D. Riebel, M. Rouble, J. E. Ruhl, E. Schaan, E. Schiappucci, N. Sehgal, C. E. Sierra, A. Simpson, B. D. Sherwin, C. Sifón, D. N. Spergel, S. T. Staggs, J. A. Sobrin, A. A. Stark, J. Stephen, C. Tandoi, B. Thorne, C. Trendafilova, C. Umilta, A. Van Engelen, J. D. Vieira, A. Vitrier, Y. Wan, N. Whitehorn, E. J. Wollack, M. R. Young, and J. A. Zebrowski, arXiv e-prints , arXiv:2504.20038 (2025), arXiv:2504.20038 [astro-ph.CO].

[11] E. Hivon, K. M. Górski, C. B. Netterfield, B. P. Crill, S. Prunet, and F. Hansen, Astrophys. J. **567**, 2 (2002), astro-ph/0105302.

[12] D. Alonso, J. Sanchez, A. Slosar, and LSST Dark Energy Science Collaboration, Mon. Not. R. Astron. Soc. **484**, 4127 (2019), 1809.09603.